HHS Public Access

Author manuscript

J Magn Reson Imaging. Author manuscript; available in PMC 2022 September 01.

Published in final edited form as:

J Magn Reson Imaging. 2021 September ; 54(3): 975–984. doi:10.1002/jmri.27623.

Voxel-level Classification of Prostate Cancer on MRI: Improving Accuracy Using Four-Compartment Restriction Spectrum Imaging

Christine H Feng, MD[1], **Christopher C Conlin, PhD**[2], **Kanha Batra, MS**[3], **Ana E Rodríguez-Soto, PhD**[2], **Roshan Karunamuni, PhD**[1], **Aaron Simon, MD, PhD**[1], **Joshua Kuperman, PhD**[2], **Rebecca Rakow-Penner, MD, PhD**[2], **Michael E Hahn, MD, PhD**[2], **Anders M Dale, PhD**[2], **Tyler M Seibert, MD, PhD**[1,2,4]

[1]Department of Radiation Medicine and Applied Sciences, UC San Diego School of Medicine, 9500 Gilman Dr, La Jolla, CA

[2]Department of Radiology, UC San Diego School of Medicine, 9500 Gilman Dr, La Jolla, CA

[3]Department of Electrical and Computer Engineering, UC San Diego, 9500 Gilman Dr, La Jolla, CA

[4]Department of Bioengineering, UC San Diego, 9500 Gilman Dr, La Jolla, CA

Abstract

Background: Diffusion MRI is integral to detection of prostate cancer (PCa), but conventional apparent diffusion coefficient (ADC) cannot capture the complexity of prostate tissues and tends to yield noisy images that do not distinctly highlight cancer. A four-compartment restriction spectrum imaging (RSI_4) model was recently found to optimally characterize pelvic diffusion signals, and the model coefficient for the slowest diffusion compartment, RSI_4-C_1, yielded greatest tumor conspicuity.

Purpose: To evaluate the slowest diffusion compartment of a four-compartment spectrum imaging model (RSI_4-C_1) as a quantitative voxel-level classifier of prostate cancer (PCa).

Study Type: Retrospective

Subjects: Forty-six men who underwent an extended MRI acquisition protocol for suspected prostate cancer. Twenty-three men had benign prostates, and the other 23 men had prostate cancer.

Field Strength/Sequence: 3T, multi-shell diffusion-weighted and axial T2-weighted sequences.

Assessment: High-confidence cancer voxels were delineated by expert consensus, using imaging data and biopsy results. The entire prostate was considered benign in patients with no detectable cancer. Diffusion images were used to calculate RSI_4-C_1 and conventional ADC. Classifier images were also generated.

Corresponding Author: Tyler Seibert, MD, PhD, Altman Clinical and Translational Research Institute, 9500 Gilman Dr. #0861, La Jolla, CA 92093, Telephone: (858) 246-5988, Fax: (844) 321-6610, tseibert@ucsd.edu.

Statistical Tests: Voxel-level discrimination of PCa from benign prostate tissue was assessed via receiver operating characteristic (ROC) curves generated by bootstrapping with patient-level case resampling. RSI_4-C_1 was compared to conventional ADC for two metrics: area under the ROC curve (AUC) and false-positive rate for a sensitivity of 90% (FPR_{90}). Statistical significance was assessed using bootstrap difference with two-sided $\alpha = 0.05$.

Results: RSI_4-C_1 outperformed conventional ADC, with greater AUC [mean 0.977 (95% CI 0.951–0.991) vs. 0.922 (0.878–0.948)] and lower FPR_{90} [0.032 (0.009–0.082) vs. 0.201 (0.132–0.290)]. These improvements were statistically significant ($p<0.05$).

Data Conclusion: RSI_4-C_1 yielded a quantitative, voxel-level classifier of PCa that was superior to conventional ADC. RSI classifier images with a low false-positive rate might improve PCa detection and facilitate clinical applications like targeted biopsy and treatment planning.

Keywords

prostate cancer; diffusion magnetic resonance imaging; restriction spectrum imaging; prostate cancer detection

INTRODUCTION

Prostate cancer is the second most frequent malignancy in men worldwide and is a common cause of cancer deaths in men (1). Strategies to improve outcomes for men with prostate cancer seek to optimize detection, staging, and clinical risk stratification. The 12-core systematic biopsy remains a common method for initial diagnosis and Gleason grading of prostate cancer, but is prone to sampling errors that can drastically influence risk stratification and treatment (2, 3). Multiparametric MRI has become increasingly popular for its added value in identifying suspicious lesions for targeted biopsy (4–7). There is also recent interest in studying its use for focal ablative treatment (8–10) or treatment escalation (11–13). We seek to improve on the limitations of clinical prostate MRI for detection of clinically significant prostate cancer using restriction spectrum imaging (RSI), a flexible framework that allows for a mixture of restricted intracellular, hindered extracellular, and freely diffusing water compartments to be probed with clinically relevant protocols (14, 15).

Clinical multiparametric MRI currently includes diffusion-weighted imaging (DWI) and apparent diffusion coefficient (ADC) maps to determine a qualitative risk of clinically significant cancer (PI-RADS v2 (16)). However, conventional ADC is a measurement of overall diffusion rate of water within a voxel and can be influenced by multiple factors. It has shown correlation with presence of malignancy, but remains limited by motion sensitivity (17), magnetic field inhomogeneity (18), and high false-positive rates from inflammation, hemorrhage, or benign lesions that limit tumor conspicuity and localization (15, 19, 20). Twenty-eight percent of PI-RADS v2 category 5 lesions (the highest level of suspicion) do not yield a diagnosis of clinically significant cancer, and false positive rates are even higher for category 3 and 4 lesions at 88% and 77.9%, respectively (21).

Advanced diffusion models use additional parameters to separate and characterize diffusion signals originating from various microstructural compartments within a voxel (22–24). The RSI technique models signal intensity as a function of *b*-value using a series of exponential

decay functions, each representing a diffusion compartment with a specific, pre-determined ADC (14, 15). Optimal compartmental ADCs were recently estimated for the prostate (and seminal vesicles) using RSI models of two to five tissue compartments (25). The overall diffusion signal was better characterized in models using more compartments, with the four-compartment model emerging as the best option by relative Bayesian information criterion (25).

The aim of this study was to apply the four-compartment RSI model to the prostate and assess voxel-level accuracy for detection of prostate cancer, with a particular focus on reducing the false positives seen on ADC.

MATERIALS AND METHODS

This study was approved with waived informed consent by the Institutional Review Board (IRB #191878).

Study Population

Eighty-one consecutive men underwent screening pelvic MRI for suspected prostate cancer between August and December 2016 using an expanded acquisition protocol (on a single scanner) that included a wider array of b-values sufficient to calculate the four-compartment RSI model. This was a retrospective study using a subset of 46 men who also had available clinical and histopathologic information. The remaining men were excluded due to incomplete information, or prior or synchronous malignancy. Standard-of-care evaluations determined that 23 men had no detectable cancer, while another 23 men had prostate cancer attributable to a PI-RADS v2 category 3–5 lesion on MRI.

MRI Data Acquisition and Post-Processing

Scans were collected on a 3T clinical MRI scanner (Discovery MR750, GE Healthcare, Waukesha, WI) using a 32-channel phased-array body coil centered on the pelvis. Each patient underwent a high-resolution, T2-weighted fast spin echo sequences with identical scan coverage as the multi-shell DWI volume (TR: 6225 ms, TE: 100 ms, resolution: 0.39×0.39 mm, matrix: 512×512, slice thickness: 3 mm). A multi-shell diffusion-weighted spin echo sequence with echo-planar imaging (EPI) readout was also acquired for each patient, sampling 5 b-values (0, 200, 1000, 2000, and 3000 s/mm^2) at 6 unique gradient directions (TR: 5000 ms, TE: 80 ms, resolution: 1.6×1.6 mm, matrix: 128×128, slice thickness: 3 mm). The $b = 0$ s/mm^2 volumes were acquired using forward and reverse phase encoding to allow for correction of B0-inhomogeneity distortions. The acquisition time for the diffusion volume was approximately 5 minutes.

Post-processing of MRI data was completed using in-house programs written in MATLAB (The MathWorks, Inc; Natick, MA). Diffusion data were corrected for distortions arising from B0 inhomogeneity, gradient nonlinearity, and eddy currents (15, 26). Conventional ADC was calculated for each voxel using distortion-corrected DWI sequences performed with b-values of 0, 200, and 1000 s/mm^2.

Prostate Data Extraction

The prostate and prostate cancer lesion regions of interest (ROIs) were contoured by consensus interpretation of a radiation oncologist, C.H.F. (3 years' experience), and two board-certified sub-specialist radiologists, R.R.P. (4 years' experience) and M.E.H. (6 years' experience), using all available clinical imaging and pathologic information. Prostate cancer ROIs were defined directly on DWI volumes using MIM (MIM Software, Inc; Cleveland, OH). Defining ROIs on DWI prevents inadvertent inclusion of benign tissue into the ROI due to subtle registration errors. The finalized ROIs were exported as binary masks into a MATLAB-compatible format that matched the resolution of the DWI volumes.

RSI Models of Prostate Diffusion

The relationship between corrected signal intensity and b-value was modeled as a linear combination of exponential decays, where $S_{corr}(b)$ represents the noise-corrected DWI signal at a particular b value, C represents signal contribution of each compartment to the overall signal, and D represents the estimated ADC value for that compartment.

$$S_{corr}(b) = C_1 e^{-bD_1} + C_2 e^{-bD_2} + C_3 e^{-bD_3} + C_4 e^{-bD_4}$$

Noise correction for DWI volumes was performed as previously described (25). Signal intensity was normalized by the median b=0 intensity within the prostate for each subject. Optimal D values for each compartment were previously determined by fitting the multi-shell DWI data from all voxels within the benign body and prostate cancer lesion ROIs (25). The compartments are ordered from lowest to highest D, with the first compartment of each model describing the most restricted mode of diffusion. Prior work has identified the four-compartment RSI model as optimally describing the diffusion signal from the prostate and prostate cancer (27). For this model, the optimal ADCs for the compartments for the full pelvic field of view were 1.0 e-4, 1.8 e-3, 3.6 e-3, and >>3.0 e-3 mm^2/s, approximately representing restricted, hindered, free diffusion, and flow, respectively (25; see Supporting Information).

Classification of Benign Prostate Tissue and Prostate Cancer

Prostate cancer conspicuity was related to the compartment with slowest diffusion in each model, called C_1, with increased cancer conspicuity for the four-compartment model. Here, C_1 for the four-compartment RSI model (RSI_4-C_1) was assessed for its ability to correctly identify benign prostate tissue and prostate cancer at the voxel level. Results with RSI were compared to those using standard ADC.

Classification of cancer and benign prostate voxels was assessed via 10,000 bootstrap samples with case resampling at the patient level to yield means and 95% confidence intervals for performance metrics. Benign subjects contributed voxels from the entire prostate, and cancer subjects contributed voxels from only the high-confidence cancer ROIs. Voxels outside the high-confidence ROIs in patients with known cancer were excluded from statistical analysis because prostate cancer is notoriously multifocal and voxel-level ground-truth histopathology was not available.

Voxel-wise classifier maps were created by the logistic regression of RSI_4-C_1 (RSI_4-C_1 classifier) using all subjects. These maps were saved in DICOM format and overlaid on the T2 volume for visualization using MIM to indicate degree of suspicion for prostate cancer. ADC maps were generated for visual comparison.

Differences in DWI accuracy between the peripheral zone (PZ) and transition zone (TZ) of the prostate are well known (16, 20, 28). Generalizable results will likely require a larger dataset. Nonetheless, an exploratory analysis was performed for prostate cancers of the PZ and TZ, respectively. For the TZ analysis, all controls were included, but any cases with PZ cancer were excluded; an analogous analysis was performed for the PZ subset. Men with cancers in both the TZ and PZ were excluded from the subset analyses.

Diffusion-weighted images, themselves, are typically interpreted qualitatively using subjective, patient-specific window/level settings. High *b*-value images do not lend themselves readily to a quantitative, voxel-level analysis without a model like the one described in the present work. Nonetheless, for comparison, we performed secondary analyses using signal intensity at each *b*-value and the same procedures to evaluate voxel-level classification.

Statistical Analysis

Voxel-level discrimination of PCa from benign prostate tissue was assessed via receiver operating characteristic (ROC) curves generated by bootstrapping with patient-level case resampling. RSI_4-C_1 was compared to conventional ADC for two metrics: area under the ROC curve (AUC) and false-positive rate for a sensitivity of 90% (FPR_{90}). Similar voxel-wise discrimination assessments were performed for cancers in TZ and PZ. Statistical significance was assessed using paired bootstrap difference with two-sided $\alpha = 0.05$.

RESULTS

Patient characteristics for cases with prostate cancer are in Table 1. Of the men with benign prostates on biopsy and/or surgical pathology, ten had PI-RADS category 1 prostates, two had PI-RADS category 2 lesions, eight had PI-RADS category 3 lesions, two had PI-RADS category 4 lesions, and one had a PI-RADS category 5 lesion.

RSI_4-C_1 outperformed conventional ADC as a quantitative, voxel-level classifier. RSI_4-C_1 had a greater AUC: mean 0.977 (95% CI 0.951–0.991), compared to 0.922 (0.878–0.948) for ADC (Figure 1A). The false positive rate was also lower for RSI_4-C_1: mean 0.032 (0.009–0.082), compared to 0.201 (0.132–0.290) for ADC (Figure 1B). Bootstrapping confirmed statistically significant differences in AUC and FPR_{90} between RSI_4-C_1 and conventional ADC ($p<0.05$ for each AUC and FPR_{90}). ROC curves for RSI_4-C_1 and ADC are presented in Figure 2 and demonstrate the improvement in false positive rate while maintaining high sensitivity. The threshold corresponding to FPR_{90} was 0.0277 for RSI_4-C_1 and 999.1 $\times 10^{-6}$ mm^2/s for ADC. The distribution of benign and cancer voxels by normalized signal intensity of RSI_4-C_1 showed less overlap between the two groups of voxels compared to that of ADC (Figure 3). RSI_4-C_1 classifier output images and conventional ADC maps for representative subjects are shown in Figure 4.

Exploratory subset analyses for prostate zones included 4 cancers in the TZ and 17 cancers in the PZ (2 patients had cancers in both the TZ and the PZ and were excluded from the subset analyses). The pattern of improved performance with RSI_4-C_1, compared to ADC, was observed in each subset. For TZ cancers, RSI_4-C_1 had AUC: mean 0.995 (95% CI 0.990–0.999), compared to 0.873 (0.794–0.950) for ADC. For TZ cancers, RSI_4-C_1 had FPR_{90}: mean 0.010 (0.002–0.022), compared to 0.286 (0.084–0.500) for ADC. Bootstrapping confirmed statistically significant differences on both metrics ($p<0.05$), but these exploratory results should be interpreted cautiously, as there were only 4 cases to draw from for bootstrapping. For PZ cancers, RSI_4-C_1 had AUC: mean 0.973 (95% CI 0.939–0.991), compared to 0.928 (0.887–0.951) for ADC. For PZ cancers, RSI_4-C_1 had FPR_{90}: mean 0.039 (0.008–0.115), compared to 0.190 (0.127–0.275) for ADC. Bootstrapping confirmed statistically significant differences ($p<0.05$) for both ADC and FPR_{90}. The distributions of benign and TZ or PZ cancer voxel values were also consistent with improved discrimination with RSI_4-C_1 (Figure 5).

Secondary analyses confirmed that DWI, alone, did not yield adequate voxel-level classification: the FPR_{90} for high *b*-value DWI (1000, 2000, and 3000 s/mm^2) was well over 0.500 in each case, compared to 0.201 and 0.032 for conventional ADC and RSI_4-C_1, respectively.

DISCUSSION

RSI_4-C_1 proved a superior voxel-level classifier for prostate cancer than conventional ADC, yielding significantly improved AUC and reduced false positives. When requiring 90% sensitivity for high-confidence cancer voxels in the cancer patients, conventional ADC performed poorly in control patients, falsely classifying approximately 1 in 5 benign voxels as cancerous. In contrast, for the same cancer sensitivity, RSI_4-C_1 gave far fewer false positives. This voxel-level classifier can be used to generate quantitative images that can be compared across subjects on the same scale and that highlight cancer with less noise (false positives) than the current imaging standard. These images may have utility in clinical applications such as MRI-guided prostate biopsy (29–31), focal ablative treatment (8–10) and targeted radiotherapy planning (11–13).

To develop the RSI model, we selected voxels that were high confidence for either benign prostate or prostate cancer, using all available clinical and pathologic information. Surgical pathology was not available for all patients, but using consecutive patients and allowing heterogeneity in type of pathology specimen avoids the selection bias of a prostatectomy-only group. High-confidence cancer voxels were chosen to avoid introducing errors into the model, as not all voxels in the cancer patients would be cancerous, but all have to be considered suspect. Conversely, it is possible that some of the clinically benign patients may have actually harbored undiagnosed cancer due to possible sampling error on biopsy. Given the high negative predictive value of clinical workup with MRI (4), the number of potential erroneous voxels within the clinically benign prostates is expected to be very small, and, if present, would only serve to dilute the effects studied here. Because we used high-confidence cancer voxels, we also expected high model performance, including high sensitivity for detecting these cancer voxels. The choice of FPR_{90} as a performance metric

reflects this expectation: when requiring 90% sensitivity for high-confidence cancer voxels, a useful model will have a low false positive rate.

The discriminatory performance of RSI_4-C_1 relies on the RSI approach of separating the overall diffusion signal into compartments believed to correspond to restricted diffusion, hindered diffusion, free water, and rapid pseudo-diffusion. A prior study demonstrated improved characterization of diffusion signal within the normal prostate and prostate tumors with this four-compartment model, especially within the most diffusion-restricted compartment, C_1 (25). By using this most restricted compartment, the vast majority of benign prostate tissue signal is suppressed, and output images have noticeably less noise than conventional ADC maps. Prior studies have also investigated the performance and utility of advanced DWI techniques, including RSI, in prostate cancer detection and characterization (23, 32–37). However, many of the other studies conducted analysis at the lesion level rather than the voxel level. A voxel-wise classifier permits generation of cancer-detecting images, like those shown in Figure 4, and avoids the need to manually define lesions. Nevertheless, distinguishing malignant and benign lesions is an important clinical problem, as is distinguishing lower and higher-grade lesions. Future work will apply the voxel-level classifier output to lesion-level analyses in a larger dataset.

Conventional ADC was calculated in this study using the most widely utilized approach consistent with PI-RADS version 2.1 (16), the consensus standard for multi-parametric prostate MRI, which recommends that ADC maps be calculated with *b*-values less than or equal to 1000 s/mm^2. Prior studies have reported increased conspicuity of prostate cancer when using *b*-values greater than 1000 s/mm^2 (38–41), and some centers—including ours—routinely acquire images with stronger diffusion weighting than that required by PI-RADS. However, the objective of the present work was to develop a quantitative, voxel-level classifier for prostate cancer. ADC is the clinical standard for quantitative diffusion MRI and so was chosen as the comparator to the quantitative model developed in this study. The inclusion of b=0 s/mm^2 may limit the accuracy of the calculated ADC due to potential microperfusion contamination at lower *b*-values(42). Nonetheless, the diffusion-weighted images, themselves, are typically interpreted qualitatively using subjective, patient-specific window/level settings. High *b*-value images do not lend themselves readily to a quantitative, voxel-level analysis without a model like the one described in the present work. Indeed, secondary analyses of the present dataset confirmed that no *b*-value yielded adequate voxel-level classification.

Limitations

We had a small sample size from a single scanner in order to take advantage of a specialized acquisition protocol, which may limit generalizability. This analysis does not compare the RSI_4 model to other advanced DWI methods or investigate the potential added value of multiple echo times (22–24, 32); we plan to acquire data adequate for these comparisons for future analyses. As mentioned above, there was also heterogeneity in pathology type, which precluded voxel-level histopathology correlation but is reflective of real-life practice patterns. There was no indication in this dataset that performance was worse for TZ cancers than PZ cancers. RSI_4-C_1 actually trended toward better performance

in the TZ, whereas ADC trended toward worse performance in the TZ, but these subset analyses for TZ cancers are considered exploratory only, as the relatively small number of cases precludes generalization. Relatively few transition zone cancers also precluded subset analysis of classifier performance by prostate zone. The overall excellent performance of our models may be partially attributed to use of majority PI-RADS category 4–5 cancers, which are already conspicuous for experienced radiologists. However, these lesions provided high-confidence training data.

Conclusion

Our study demonstrated that RSI_4-C_1 yields a voxel-level classifier of prostate cancer that is superior to conventional ADC. RSI classifier images, with a lower false-positive rate, might be used to assist in accurate detection of prostate cancer. A pending clinical trial (ClinicalTrials.gov #NCT04349501) will apply this RSI_4-C_1 classifier to prospective data and evaluate this quantitative metric for treatment response assessment.

Supplementary Material

Refer to Web version on PubMed Central for supplementary material.

ACKNOWLEDGEMENTS

The authors acknowledge Dr. Nathan White for his contribution to the framework of restriction spectrum imaging and guidance.

Grant Support: This work was supported by funding from the following sources: USAMR DoD W81XWH-17–1-0618, NIH K08 NIBIB EB026503, Prostate Cancer Foundation, UC San Diego Center for Precision Radiation Medicine.

REFERENCES

1. Bray F, Ferlay J, Soerjomataram I, Siegel RL, Torre LA, Jemal A: Global cancer statistics 2018: GLOBOCAN estimates of incidence and mortality worldwide for 36 cancers in 185 countries. CA Cancer J Clin2018; 68:394–424. [PubMed: 30207593]
2. Hu Y, Ahmed HU, Carter T, et al.: A biopsy simulation study to assess the accuracy of several transrectal ultrasonography (TRUS)-biopsy strategies compared with template prostate mapping biopsies in patients who have undergone radical prostatectomy. BJU Int2012; 110:812–820. [PubMed: 22394583]
3. Carter HB, Albertsen PC, Barry MJ, et al.: Early detection of prostate cancer: AUA Guideline. J Urol2013; 190:419–26. [PubMed: 23659877]
4. Ahmed HU, El-Shater Bosaily A, Brown LC, et al.: Diagnostic accuracy of multi-parametric MRI and TRUS biopsy in prostate cancer (PROMIS): a paired validating confirmatory study. Lancet (London, England)2017; 389:815–822.
5. Rouvière O, Puech P, Renard-Penna R, et al.: Use of prostate systematic and targeted biopsy on the basis of multiparametric MRI in biopsy-naive patients (MRI-FIRST): a prospective, multicentre, paired diagnostic study. Lancet Oncol2019; 20:100–109. [PubMed: 30470502]
6. Ahdoot M, Wilbur AR, Reese SE, et al.: MRI-targeted, systematic, and combined biopsy for prostate cancer diagnosis. N Engl J Med2020; 382:917–928. [PubMed: 32130814]
7. Kasivisvanathan V, Rannikko AS, Borghi M, et al.: MRI-Targeted or Standard Biopsy for Prostate-Cancer Diagnosis. N Engl J Med2018; 378:1767–1777. [PubMed: 29552975]
8. Ahmed HU, Dickinson L, Charman S, et al.: Focal Ablation Targeted to the Index Lesion in Multifocal Localised Prostate Cancer: a Prospective Development Study. Eur Urol2015; 68:927–936. [PubMed: 25682339]

9. Elkhoury FF, Simopoulos DN, Marks LS: MR-guided biopsy and focal therapy: new options for prostate cancer management. Curr Opin Urol2018; 28:93–101. [PubMed: 29232269]
10. Le Nobin J, Rosenkrantz AB, Villers A, et al.: Image Guided Focal Therapy for Magnetic Resonance Imaging Visible Prostate Cancer: Defining a 3-Dimensional Treatment Margin Based on Magnetic Resonance Imaging Histology Co-Registration Analysis. J Urol2015; 194:364–370. [PubMed: 25711199]
11. McDonald AM, Dobelbower MC, Yang ES, et al.: Prostate Stereotactic Body Radiation Therapy With a Focal Simultaneous Integrated Boost: Acute Toxicity and Dosimetry Results From a Prospective Trial. Adv Radiat Oncol2018; 4:90–95. [PubMed: 30706015]
12. Bauman G, Haider M, Van der Heide UA, Ménard C: Boosting imaging defined dominant prostatic tumors: a systematic review. Radiother Oncol J Eur Soc Ther Radiol Oncol2013; 107:274–281.
13. Murray LJ, Lilley J, Thompson CM, et al.: Prostate stereotactic ablative radiation therapy using volumetric modulated arc therapy to dominant intraprostatic lesions. Int J Radiat Oncol Biol Phys2014; 89:406–415. [PubMed: 24685447]
14. White NS, Dale AM: Distinct effects of nuclear volume fraction and cell diameter on high b-value diffusion MRI contrast in tumors. Magn Reson Med2014; 72:1435–43. [PubMed: 24357182]
15. White NS, McDonald CR, Farid N, et al.: Diffusion-weighted imaging in cancer: Physical foundations and applications of restriction spectrum imaging. Cancer Res2014:4638–4652. [PubMed: 25183788]
16. Turkbey B, Rosenkrantz AB, Haider MA, et al.: Prostate Imaging Reporting and Data System Version 2.1: 2019 Update of Prostate Imaging Reporting and Data System Version 2. Eur Urol2019; 76:340–351. [PubMed: 30898406]
17. Kallehauge JF, Tanderup K, Haack S, et al.: Apparent Diffusion Coefficient (ADC) as a quantitative parameter in diffusion weighted MR imaging in gynecologic cancer: Dependence on b-values used. Acta Oncol (Madr)2010; 49:1017–1022.
18. Koh D-M, Takahara T, Imai Y, Collins DJ: Practical aspects of assessing tumors using clinical diffusion-weighted imaging in the body. Magn Reson Med Sci2007; 6:211–24. [PubMed: 18239358]
19. Hoeks CMA, Barentsz JO, Hambrock T, et al.: Prostate Cancer: Multiparametric MR Imaging for Detection, Localization, and Staging. Radiology2011; 261:46–66. [PubMed: 21931141]
20. Hoeks CMA, Vos EK, Bomers JGR, Barentsz JO, Hulsbergen-Van De Kaa CA, Scheenen TW: Diffusion-weighted magnetic resonance imaging in the prostate transition zone: Histopathological validation using magnetic resonance-guided biopsy specimens. Invest Radiol2013; 48:693–701. [PubMed: 23614975]
21. Mehralivand S, Bednarova S, Shih JH, et al.: Prospective Evaluation of PI-RADS™ Version 2 Using the International Society of Urological Pathology Prostate Cancer Grade Group System. J Urol2017; 198:583–590. [PubMed: 28373133]
22. Panagiotaki E, Walker-Samuel S, Siow B, et al.: Noninvasive Quantification of Solid Tumor Microstructure Using VERDICT MRI. Cancer Res2014; 74:1902–1912. [PubMed: 24491802]
23. Chatterjee A, Bourne RM, Wang S, et al.: Diagnosis of Prostate Cancer with Noninvasive Estimation of Prostate Tissue Composition by Using Hybrid Multidimensional MR Imaging: A Feasibility Study. Radiology2018; 287:864–873. [PubMed: 29393821]
24. Felker ER, Raman SS, Shakeri S, et al.: Utility of restriction spectrum imaging among men undergoing first-time biopsy for suspected prostate cancer. Am J Roentgenol2019; 213:365–370. [PubMed: 31039011]
25. Conlin CC, Feng CH, Rodríguez-Soto AE, et al.: Improved characterization of diffusion in normal and cancerous prostate tissue through optimization of the restriction spectrum imaging signal model. medRxiv2020:2020.03.27.20042069.
26. Holland D, Kuperman JM, Dale AM: Efficient correction of inhomogeneous static magnetic field-induced distortion in Echo Planar Imaging. Neuroimage2010; 50:175–183. [PubMed: 19944768]
27. Conlin CC, Feng CH, Rodriguez-Soto AE, et al.: Improved Characterization of Diffusion in Normal and Cancerous Prostate Tissue Through Optimization of Multicompartmental Signal Models. J Magn Reson Imaging2020:1–12.

28. Chatterjee A, Watson G, Myint E, Sved P, McEntee M, Bourne R: Changes in epithelium, stroma, and lumen space correlate more strongly with gleason pattern and are stronger predictors of prostate ADC changes than cellularity metrics1. Radiology2015; 277:751–762. [PubMed: 26110669]
29. Tewes S, Peters I, Tiemeyer A, et al.: Evaluation of MRI/Ultrasound Fusion-Guided Prostate Biopsy Using Transrectal and Transperineal Approaches. Biomed Res Int2017; 2017:2176471. [PubMed: 29094042]
30. Marks L, Young S, Natarajan S: MRI-ultrasound fusion for guidance of targeted prostate biopsy. Curr Opin Urol2013; 23:43–50. [PubMed: 23138468]
31. Kongnyuy M, George AK, Rastinehad AR, Pinto PA: Magnetic Resonance Imaging-Ultrasound Fusion-Guided Prostate Biopsy: Review of Technology, Techniques, and Outcomes. Curr Urol Rep2016; 17:32. [PubMed: 26902626]
32. Le Bihan D, Breton E, Lallemand D, Aubin ML, Vignaud J, Laval-Jeantet M: Separation of diffusion and perfusion in intravoxel incoherent motion MR imaging. Radiology1988; 168:497–505. [PubMed: 3393671]
33. Johnston EW, Bonet-Carne E, Ferizi U, et al.: VERDICT MRI for Prostate Cancer: Intracellular Volume Fraction versus Apparent Diffusion Coefficient. Radiology2019; 291:391–397. [PubMed: 30938627]
34. Chatterjee A, Harmath C, Oto A: New prostate MRI techniques and sequences. Abdom Radiol2020.
35. Rakow-Penner RA, White NS, Parsons JK, et al.: Novel technique for characterizing prostate cancer utilizing MRI restriction spectrum imaging: proof of principle and initial clinical experience with extraprostatic extension. Prostate Cancer Prostatic Dis2015; 18:81–85. [PubMed: 25559097]
36. McCammack KC, Kane CJ, Parsons JK, et al.: In vivo prostate cancer detection and grading using restriction spectrum imaging-MRI. Prostate Cancer Prostatic Dis2016; 19:168–173. [PubMed: 26754261]
37. McCammack KC, Schenker-Ahmed NM, White NS, et al.: Restriction spectrum imaging improves MRI-based prostate cancer detection. Abdom Radiol2016; 41:946–953.
38. Grant KB, Agarwal HK, Shih JH, et al.: Comparison of calculated and acquired high b-value diffusion weighted imaging in prostate cancer. Abdom Imaging2015; 40:578. [PubMed: 25223523]
39. Tamada T, Kanomata N, Sone T, et al.: High b Value (2,000 s/mm2) Diffusion-Weighted Magnetic Resonance Imaging in Prostate Cancer at 3 Tesla: Comparison with 1,000 s/mm2 for Tumor Conspicuity and Discrimination of Aggressiveness. PLoS One2014; 9.
40. Maas MC, Fütterer JJ, Scheenen TWJ: Quantitative Evaluation of Computed High b Value Diffusion-Weighted Magnetic Resonance Imaging of the Prostate. Invest Radiol2013; 48:779–786. [PubMed: 23907102]
41. Metens T, Miranda D, Absil J, Matos C: What is the optimal b value in diffusion-weighted MR imaging to depict prostate cancer at 3T?Eur Radiol2012; 22:703–709. [PubMed: 21971824]
42. Le Bihan D, Turner R, Moonen CTW, Pekar J: Imaging of diffusion and microcirculation with gradient sensitization: Design, strategy, and significance. J Magn Reson Imaging1991:7–28. [PubMed: 1802133]
43. Armstrong AJ, Victor AD, Davis BJ, et al.: NCCN Guidelines Version 2.2019 Prostate Cancer. 2019.

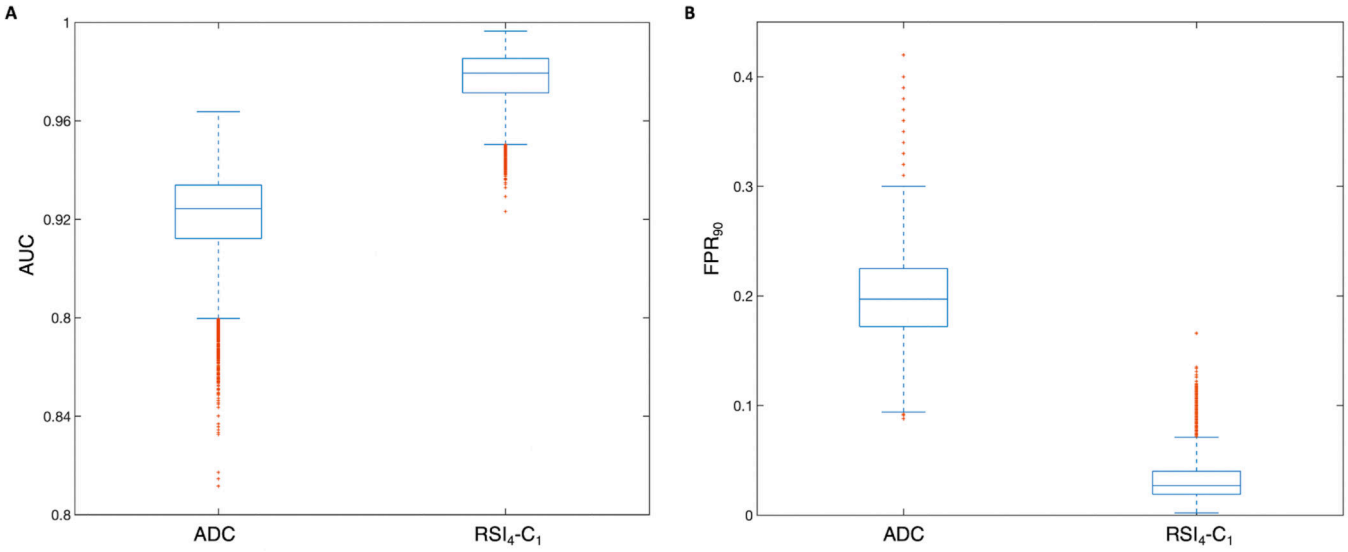

Figure 1.

Box plots depicting distribution of performance metrics for 10,000 patient-level bootstrap samples for A) area under the curve (AUC) and B) the false positive rate at 90% sensitivity (FPR_{90}) for conventional ADC and RSI_4-C_1. Whiskers represent values within 1.5 times the interquartile range (IQR).

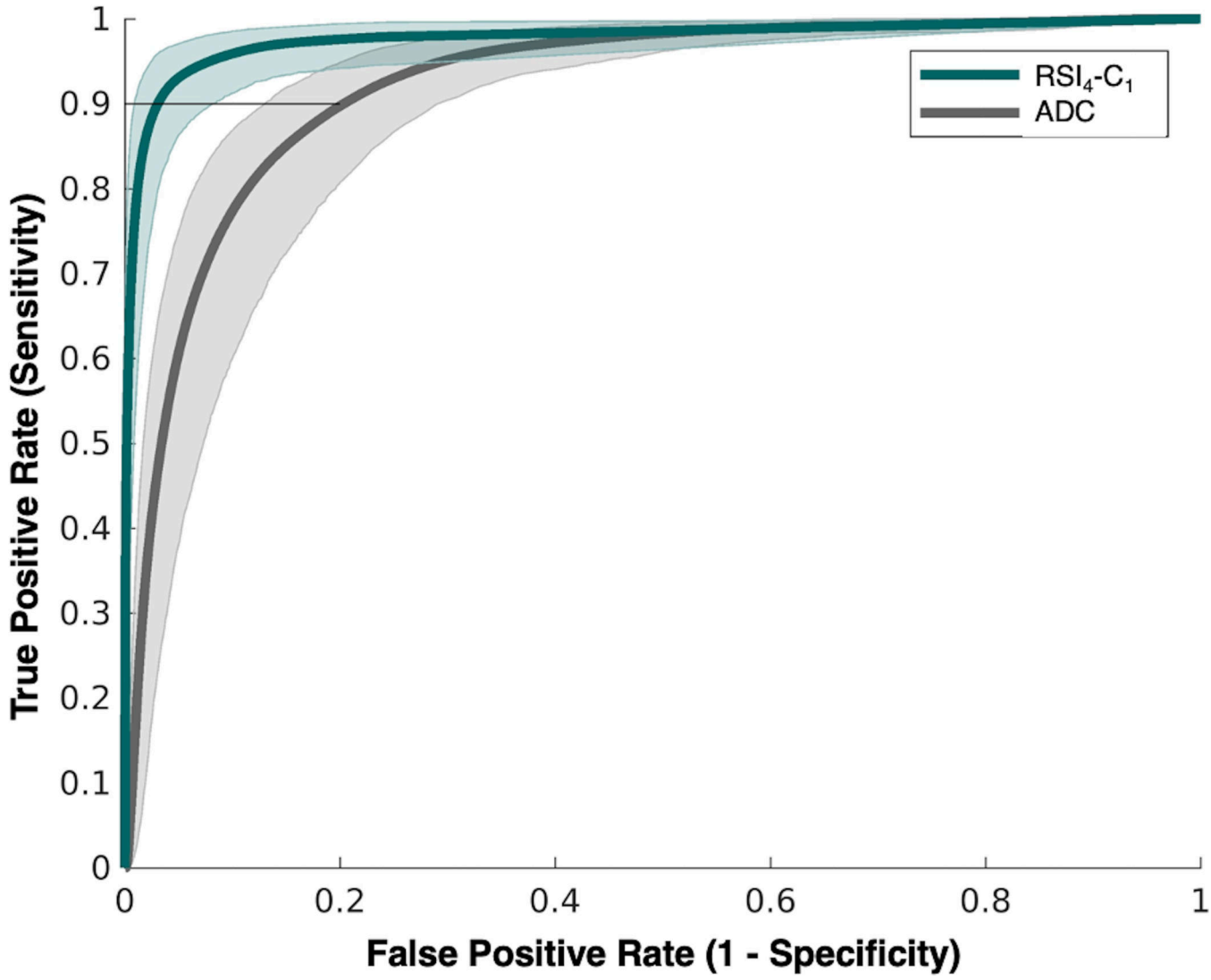

Figure 2.

Receiver operating characteristic (ROC) curves for conventional ADC (grey) and RSI_4-C_1 (green) with confidence intervals indicated by shaded areas. FPR_{90} is highlighted by a horizonal line at 0.9 sensitivity, with corresponding coordinate along the x-axis indicating false positive rate.

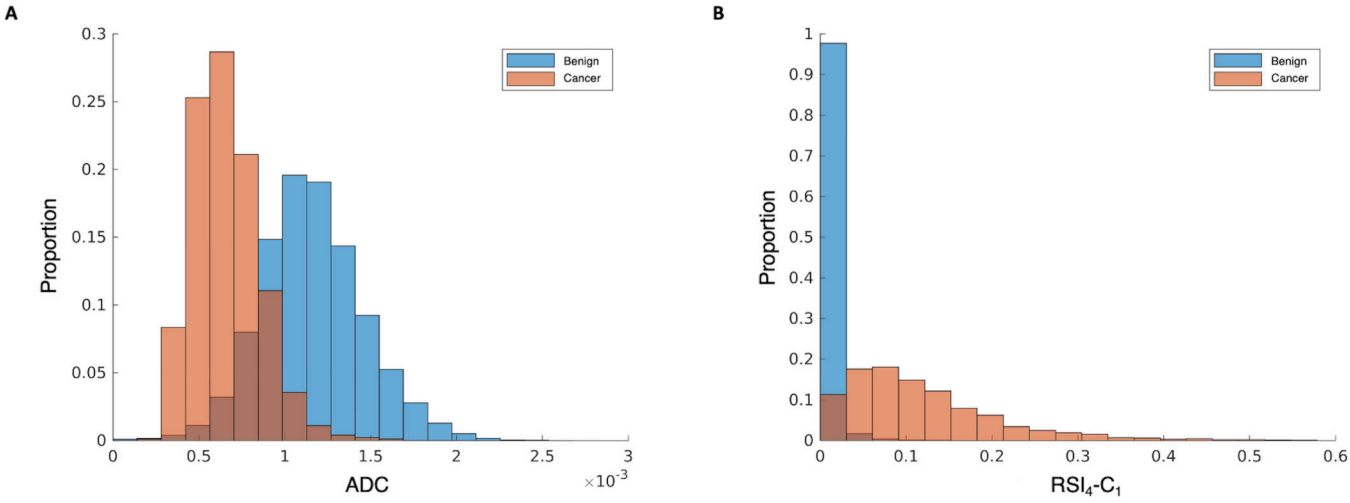

Figure 3.

Normalized histograms of signal intensity for A) conventional ADC and B) RSI_4-C_1. Benign voxels are shown in blue and cancer voxels are in orange, with the overlapping regions in brown. RSI_4-C_1 has less overlap in the distribution of benign and cancer voxels compared to ADC.

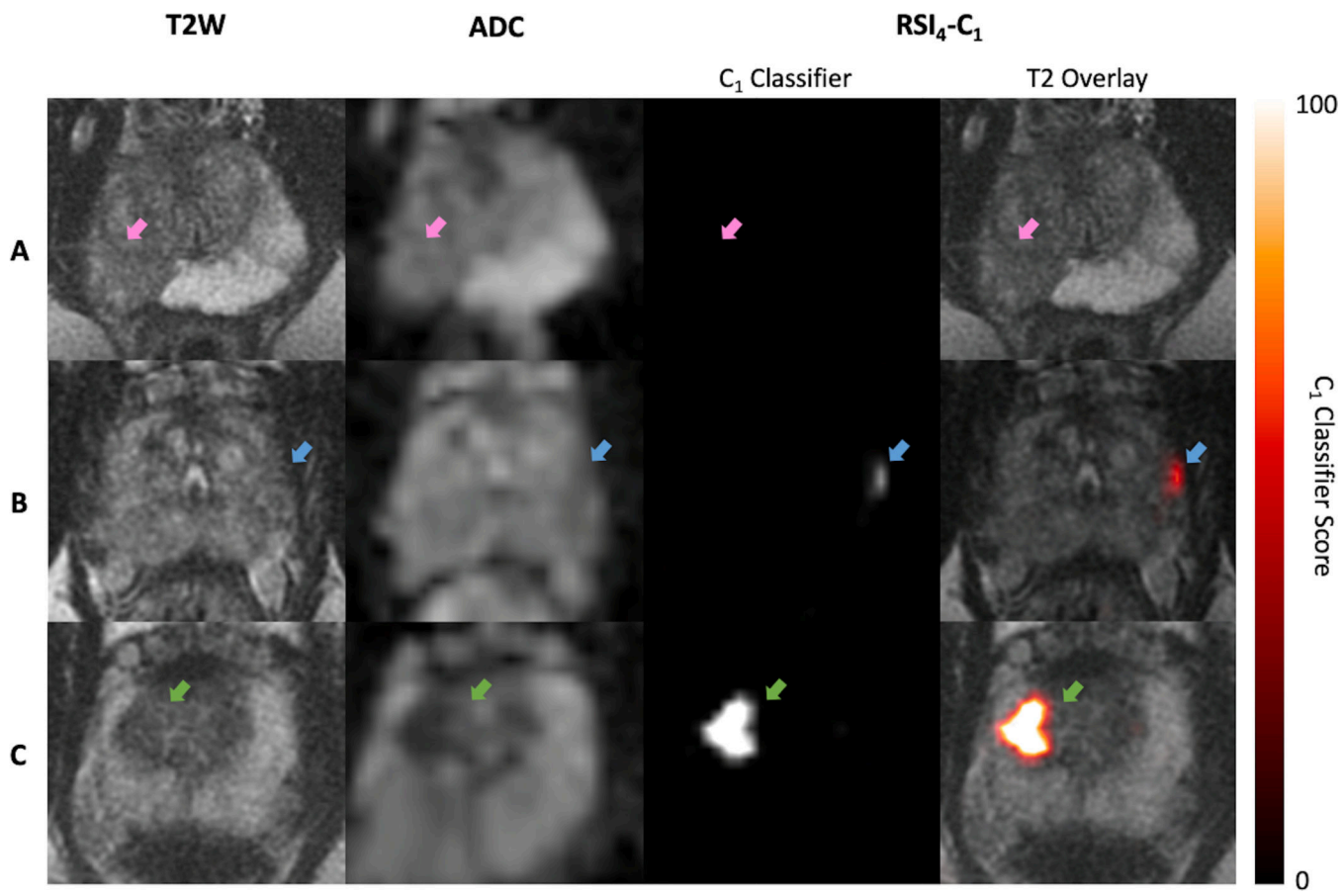

Figure 4.

Representative axial images of T2-weighted MRI (T2W), conventional ADC, and logistic regression of RSI_4-C_1 (RSI_4-C_1 classifier) for 3 representative subjects. Subject A had a PI-RADS 5 lesion (pink arrow) on MRI, with two subsequent negative biopsies showing only acute and chronic inflammation. Subject B had a small PI-RADS 3 lesion (blue arrow) in the left peripheral zone; he underwent radical prostatectomy and was found to have Gleason 3+4 prostate cancer with focal extraprostatic extension. Subject C had a PI-RADS 3 lesion (green arrow) in the right transition zone; he underwent prostatectomy and was found to have Gleason 4+3+5 prostate cancer. RSI_4-C_1 classifier maps readily highlight the cancers for subjects B and C. The RSI_4-C_1 classifier map for subject A has no false-positive voxels; it is shown on the same color scale as the maps for subjects B and C.

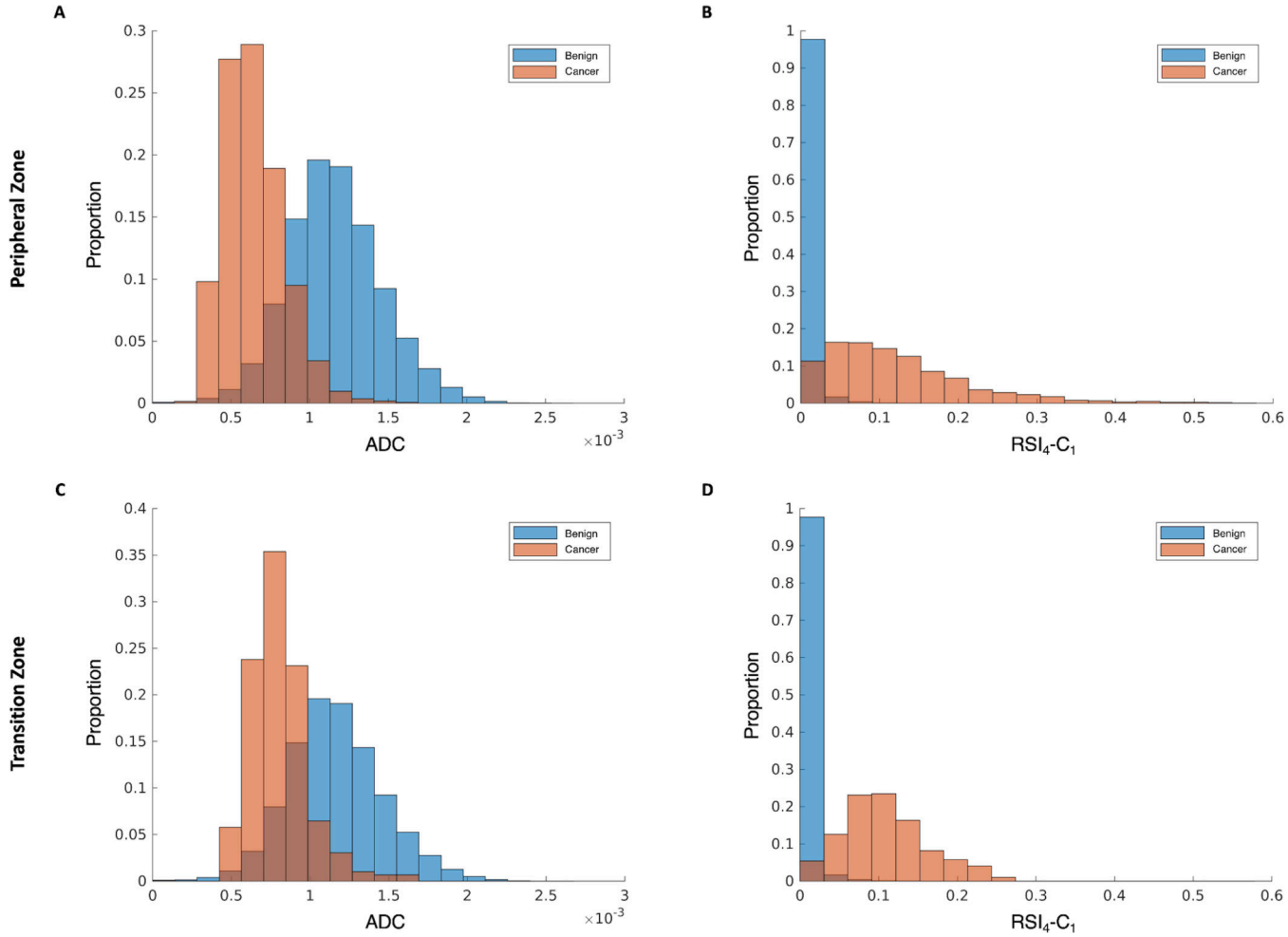

Figure 5.

Normalized histograms of signal intensity from subset analyses of peripheral zone (top row) and transition zone (bottom row) for conventional ADC (panels A & C) and RSI_4-C_1 (panels B &D). Benign voxels are shown in blue and cancer voxels in orange, with the overlapping regions in brown. RSI_4-C_1 has less overlap in the distribution of benign and cancer voxels compared to ADC when using subsets of cancers in the peripheral zone or transition zone.

Table 1.

Characteristics of cases with prostate cancer. Clinical risk groups were designated per NCCN guidelines(43) for favorable intermediate risk (FIR), unfavorable intermediate risk (UIR), high risk (HR), and very high risk (VHR).

Case	Age	PI-RADS v2	Lesion Location	PSA (ng/mL)	Gleason Score	Gleason Grade Group	Pathology Specimen Type	Stage	Clinical Risk Group
1	59	5	Right Transition & Peripheral Zones	7.77	3+4	2	Biopsy (Systematic prior to MRI)	cT1cN0	FIR
2	54	5	Right Peripheral Zone	10.6	4+3	3	Biopsy (Systematic prior to MRI), Radical Prostatectomy	pT3aN0	UIR
3	71	5	Right Peripheral & Transition Zones	4.04	4+5	5	Biopsy (Systematic and Targeted), Radical Prostatectomy	pT3aN0	HR
4	72	5	Right Peripheral Zone	5.7	3+4	2	Biopsy (Systematic prior to MRI)	cT2bN0	UIR
5	54	5	Right Peripheral Zone	7.3	4+3	3	Biopsy (Systematic prior to MRI), Radical Prostatectomy	pT3aN0	HR
6	63	5	Right Peripheral Zone	16.83	4+3	3	Biopsy (Systematic prior to MRI), Radical Prostatectomy	pT3aN0	HR
7	74	5	Right Peripheral Zone	29.3	4+5	5	Biopsy (Systematic prior to MRI)	cT2cN0	HR
8	53	4	Left Peripheral Zone	8	3+3	1	Biopsy (Systematic prior to MRI), Radical Prostatectomy	pT2cN0	FIR
9	66	4	Right Peripheral Zone	8.66	4+3	3	Biopsy (Systematic and Targeted)	cT1cN0	UIR
10	67	5	Left Peripheral Zone	4.6	3+4	2	Biopsy (Systematic and Targeted)	cT1cN0	FIR
11	62	5	Left Peripheral Zone	13.97	4+3	3	Biopsy (Systematic prior to MRI), Radical Prostatectomy	pT3aN0	HR
12	74	4	Left Peripheral Zone	4.4	4+3	3	Biopsy (Systematic and Targeted), Radical Prostatectomy	pT2aN0	UIR
13	50	3	Left Peripheral Zone	4.3	3+4	2	Biopsy (Systematic prior to MRI), Radical Prostatectomy	pT3aN0	HR
14	65	4	Right Transition Zone	8	3+3	1	Biopsy (Systematic prior to MRI)	cT1cN0	LR
15	81	5	Anterior Transition Zone	8.5	3+4	2	Biopsy (Systematic and Targeted)	cT2aN0	FIR
16	77	5	Right Peripheral Zone	3.47	4+4	4	Biopsy (Systematic), Radical Prostatectomy	ypT2aN0	HR
17	70	4	Left Peripheral Zone	7.43	3+4	2	Biopsy (Systematic and Targeted)	cT1cN0	FIR
18	58	4	Left Peripheral Zone	7.42	3+4	2	Biopsy (Systematic and Targeted), Radical Prostatectomy	mpT2cN0	UIR
19	62	4	Left Peripheral Zone	5	3+3	1	Biopsy (Systematic prior to MRI)	cT1cN0	LR

Case	Age	PI-RADS v2	Lesion Location	PSA (ng/mL)	Gleason Score	Gleason Grade Group	Pathology Specimen Type	Stage	Clinical Risk Group
20	68	4	Right Peripheral Zone	5.9	4+5	5	Biopsy (Systematic and Targeted), Radical Prostatectomy	mpT2cN0	HR
21	64	5	Midline to Right Transition Zone	8.63	3+4	2	Biopsy (Systematic and Targeted)	cT1cN0	FIR
22	51	5	Diffuse Peripheral Zone	33	4+5	5	Biopsy (Systematic prior to MRI)	ypT3bN0	VHR
23	51	3	Right Transition Zone	5.42	4+3+5	3	Biopsy (Systematic prior to MRI), Radical Prostatectomy	pT2bN0	UIR